eJSSNT Regular Paper

e-Journal of Surface Science and Nanotechnology **23**, 119–131 (2025)

First-principles Study of Intrinsic hBN Island Nucleated During CVD Initial Growth on Cu(111)

Ryo Imamura, Insung Seo, Hiroyuki Kageshima †

Graduate School of Natural Science and Technology, Shimane University, 1060 Nishi-Kawatsucho, Matsue, Shimane 690-8504, Japan
† *Corresponding author: kageshima@riko.shimane-u.ac.jp*

Received: 10 January, 2025; Accepted: 10 March, 2025; J-STAGE Advance Publication: 12 April, 2025; Published: 12 April, 2025

The initial growth mechanisms of intrinsic hexagonal boron nitride (hBN) islands on Cu(111) terraces during chemical vapor deposition (CVD) are investigated using density functional theory calculations. Edge energies are calculated with high accuracy, and critical sizes for previously unexamined island shapes are predicted. The formation energies of small hBN islands are found to be strongly influenced by the curl effect. Through two-dimensional variation of the chemical potential, three of the most stable structures at the critical size—zigzag hexagonal, zigzag boron-edge triangular, and zigzag nitrogen-edge triangular—are identified. Generalization of these shapes enables the drawing of two types of phase diagrams, demonstrating a strong dependence of shape stability on the chemical potential. It is further revealed that maintaining the chemical potential near a specific value is essential for increasing the critical size. These results provide explanations for the experimentally observed hBN island shapes on Cu surfaces during CVD and propose chemical potential conditions for growing hBN films with superior single crystallinity.

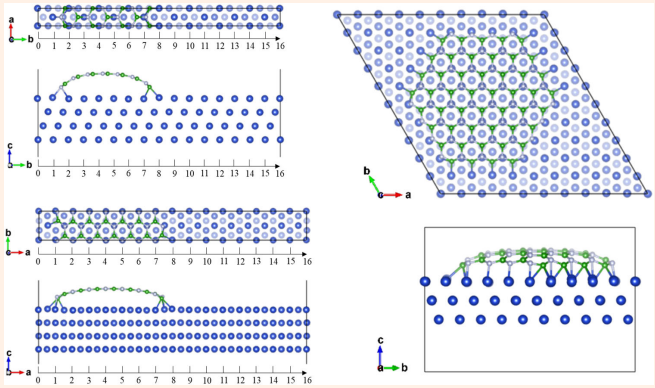

Keywords *Hexagonal boron nitride; Chemical vapor deposition; First-principles calculation; Critical size; Chemical potential*

I. INTRODUCTION

Hexagonal boron nitride (hBN) is a two-dimensional (2D) material with a honeycomb structure composed of sp^2 hybridized covalent bonds between B and N atoms. It exhibits a bandgap of 5.97 eV [1, 2]. Bulk hBN possesses exceptional mechanical and thermal strength, as well as high chemical stability [3, 4]. These properties make hBN highly suitable as an insulating layer for electronics based on 2D semiconductor materials, such as graphene and transition metal dichalcogenides (TMDCs). In the field of 2D transistor research, devices combining hBN flakes—mechanically exfoliated from hBN crystals synthesized via high-pressure and high-temperature (HP/HT) methods—with graphene and TMDCs have been extensively studied. To date, the flattening effect of hBN at interfaces has been reported to enable high carrier mobility and reduce charge trapping [5–9].

hBN mechanically exfoliated from crystals synthesized via HP/HT methods exhibits exceptional quality in terms of film uniformity and thickness control. However, its lateral size is limited to several tens of micrometers [6–8]. In contrast, chemical vapor deposition (CVD) methods using borazine ($B_3N_3H_6$) or ammonia borane (BH_3-NH_3) as precursors enable the growth of hBN over large areas at low cost [10, 11]. For industrial applications, achieving both large-area coverage and cost-effective production is highly desirable. Nevertheless, the quality of CVD-grown hBN remains inferior to that of mechanically exfoliated hBN derived from HP/HT-synthesized crystals. For practical applications of CVD-grown hBN, its quality must be comparable to or surpass that of exfoliated hBN. Therefore, improving the quality of CVD-grown hBN is crucial to unlocking its potential for industrial applications.

In the CVD growth of hBN, the choice of catalytic metal substrate plays a critical role in controlling film thickness. For instance, when substrates like Ni or Ni-Fe alloys, which exhibit high solubility for B and N, are used, hBN tends to grow into multilayers via precipitation reactions [11–13].

In contrast, substrates such as Cu, Co, Pt, Ru, and Ir do not promote precipitation reactions, resulting in the growth of monolayer hBN [10, 14–26]. During CVD growth on Cu(111), it has been reported that hBN forms triangular islands [10, 14, 19–21, 23–26]. However, under specific conditions, such as when the Cu surface is pretreated by electropolishing [19] or when a small amount of O_2 is mixed with the carrier gas [26], hexagonal islands are observed. To date, the successful growth of high-quality single-crystalline hBN has been achieved primarily through the optimization of growth temperature, substrate conditions, precursor types and dosages, and carrier gas types and flow rates. Chen *et al.* [10] reported the growth of wafer-scale, large-area, high-quality monolayer hBN films via low-pressure CVD with BH_3-NH_3 as the raw material on a Cu(111) thin film on sapphire, without grain boundaries, at a growth temperature of 1050°C. Notably, the islands formed during growth were triangular in shape, with almost all aligned in the same orientation. Since hBN exhibits three-fold symmetry, Cu(111), which also exhibit three-fold symmetry, is considered an ideal substrate orientation. Achieving superior single crystallinity requires precise control over the growth temperature—set as close as possible to the substrate's melting point—and minimizing the raw material dosage.

From an industrial application perspective, achieving the growth of larger-area hBN films with superior quality remains a significant challenge. To address this, it is crucial to gain a detailed understanding of the growth mechanism of hBN crystals on Cu(111). We have investigated the crystal growth mechanism of hBN using first-principles calculations based on density functional theory (DFT). Specifically, we focused on the critical size, a key factor that determines the nucleation density during crystal growth. Exploring the conditions that lead to a larger critical size is closely linked to achieving higher-quality single-crystalline hBN growth.

In previous theoretical studies, the relationship between the shape of hBN islands on Cu(111) and the chemical potential has been discussed [27, 28]. These studies assumed macroscopic hBN sizes and examined the stability of shapes based on edge energy per unit length. As a result, it was concluded that the N-terminated triangular shape is stable under the condition of the N-rich side, while the B-terminated triangular shape is stable under the condition of the B-rich side. However, these scenarios focus on stable shapes and do not provide insights into strategies for growing high-quality crystals. Furthermore, Fan *et al.* [24] conducted a study on hBN growth via CVD on Cu(111) from both experimental and theoretical perspectives, while they did not investigate the growth process based on the critical size.

We have conducted theoretical studies aimed at discussing strategies for growing high-quality crystals, particularly by examining the critical size. In our previous theoretical study [29], we created a model assuming various shapes of hBN nucleation on an ideal terrace of Cu(111) and calculated their total energies. From these calculations, we evaluated the formation energy (E_f) and investigated the relationship between the edge-B energy (ε_B), edge-N energy (ε_N), and the energy of the inside atoms that are not at the edges (ε_{in}). Using these three variables, we predicted the critical size at which hBN nuclei would spontaneously begin to grow, based on a mathematical approach. However, three key issues were identified: 1) The three variables could only predict the critical size for hBN nuclei in the shape of a triangle. 2) These variables include effects specific to small islands, which have not been fully examined, and there should be concern about the quantitative validity of these three variables. 3) The range of chemical potentials used in the analysis of the results was one-dimensional, allowing for only limited comparison with experimental results.

In this study, we conducted theoretical research to address these issues. Using a nanoribbon hBN model on Cu(111), we evaluated the energy for the zigzag (Z) edge and the armchair (A) edge, denoted as ε_Z and ε_A, respectively, based on the results for nanoribbons with these edge types. This approach enabled us to predict the critical size for shapes other than triangles. By performing calculations on sufficiently wide nanoribbons, the number of inside atoms with the ideal value of ε_{in} was increased, and the average value of ε_{in} approached the ideal value. In other words, the curl effect [29] became negligible. Furthermore, by considering the 2D variation of the chemical potential, we were able to compare the results with experimental observations in greater detail and discuss the conditions for increasing the critical size. The results reveal that the most stable structure at the critical size varies significantly depending on the chemical potential and that targeting a specific, narrow range of chemical potential is essential for increasing the critical size.

II. METHODOLOGY

We performed the DFT calculations using the PHASE/0 program package [30]. All calculations were based on the projector augmented wave (PAW) method, employing PAW ultrasoft pseudopotentials. The cutoff energy for the plane-wave basis was set to 30 Ry, and van der Waals corrections were introduced using the rev-vdW-DF2 (B86r) functional [31]. This functional has been demonstrated to accurately reproduce the interlayer spacing of bulk hBN [31], and is the only correction reported to reproduce the experimental moiré pattern of hBN/Ir(111) [32]. Thus, B86r is suitable for hBN on metal surfaces.

Given its widespread experimental use, we chose the Cu(111) surface for our calculations. The Monkhorst-Pack scheme was employed for *k*-point sampling. Convergence criteria for electronic energy and forces were set to 10^{-10} hartree and 10^{-3} hartree bohr^{-1}, respectively. For the structure where the entire Cu(111) surface is fully covered by an hBN sheet (without edges), referred to as the full coverage hBN on the Cu(111) system, these criteria were adjusted to 10^{-10} hartree and 2×10^{-4} hartree bohr^{-1}, respectively. While certain atoms were fixed at specific positions, the positions of all other atoms were optimized.

The B atom was placed at the hollow site, directly above the third Cu layer from the surface, and the N atom was

positioned at the top site, directly above a surface Cu atom. It is known that this configuration is the most energetically stable pattern under the condition of B86r functional [29]. The formation energy E_f was defined as

$$E_f = E_{tot} - E_{Cu} - n_B\mu_B - n_N\mu_N, \quad (1)$$

where E_{tot} and E_{Cu} are the total energies of the system with the hBN island adsorbed and of the bare Cu substrate, respectively. n_B and n_N represent the number of B and N atoms in the island. μ_B and μ_N indicate the chemical potential of B and of N.

In our previous work [29], we considered a one-dimensional constraint in which μ_B and μ_N were linked, analogous to studies on the epitaxial growth of GaAs and GaN [33, 34]. However, unlike GaAs and GaN, hBN does not grow on an hBN substrate but rather on a Cu substrate. Consequently, the supply of N does not necessarily ensure a corresponding supply of B in an appropriate ratio. Instead, the B and N precursors are likely to behave independently.

Thus, we defined μ_B and μ_N as

$$\mu_B = E_{Batom} + \Delta\mu_B, \quad (2)$$

$$\mu_N = E_{Natom} + \Delta\mu_N, \quad (3)$$

where E_{Batom} and E_{Natom} are the energies of the isolated B and N atoms, which are −149.07 and −377.62 eV, respectively. $\Delta\mu_B$ and $\Delta\mu_N$ denote the variations in μ_B and μ_N. The upper limits of μ_B and μ_N are set to E_{Batom} and E_{Natom}, respectively, implying in $\Delta\mu_B$ and $\Delta\mu_N$ are less than or equal to zero. To explore the broadest possible range of variation, we set the upper limits of μ_B and μ_N to the energies of isolated atomic states, which are the most unstable phases. A conceptual diagram of the chemical potential range defined by Eqs. (2) and (3) is shown in Figure S1 in Supplementary Material. In this study, we assume that μ_B and μ_N can vary freely and treat $\Delta\mu_B$ and $\Delta\mu_N$ as variables constrained to ≤ 0. Through this approach, the chemical potentials are defined as variables with 2D degrees of freedom, as described by Eqs. (2) and (3). While the lower limits of $\Delta\mu_B$ and $\Delta\mu_N$ are not well understood, we set them to −10 eV to explore the widest possible range.

In our previous study [29], we defined the chemical potentials under the condition of $\mu_B + \mu_N = E_{BN}$, where E_{BN} describes the energy per BN pair in a free-standing hBN sheet, which is −541.034 eV. The upper limit of μ_B is given by the energy per atom of α-boron, $E_{\alpha B}/50 = -155.70$ eV, while the upper limit of μ_N by half the energy of an N_2 molecule, $E_{N_2}/2 = -382.60$ eV. Under these conditions, the lower limits of μ_B and μ_N are −158.40 and −385.28 eV, respectively. The midpoint values between the upper and lower limits of μ_B and μ_N (corresponding to $\overline{\mu}_N = 0.5$ in Ref. 29) are associated with $\Delta\mu_B = -8.01$ eV and $\Delta\mu_N = -6.34$ eV in this study. The chemical potential range considered in our previous study is also shown in Figure S1. It is evident that the range was extremely narrow.

A. Nanoribbon model

Z and A nanoribbon models are shown in Figure 1. The reason why we considered these models is to evaluate ε_Z and ε_A under the condition of ideal value of ε_{in}, thereby improving the precision of critical size evaluations. For the Z and A nanoribbon hBN, Cu(111) $1 \times 8\sqrt{3}$ and $16 \times \sqrt{3}$ orthorhombic lateral supercells were adopted, respectively (Figure 1). In both cases, a super-slab geometry with a vacuum layer of 11 Å was applied, and the slab thickness was set to four Cu layers, with the bottom layer fixed. The k-point grid was $12 \times 1 \times 1$ for the Z nanoribbon and $1 \times 6 \times 1$ for the A nanoribbon. By counting the number of six-membered rings in the width of nanoribbons, denoted as n_t, n_t was varied from 3 to 13 in increments of one, and the corresponding E_f was calculated for each case. To evaluate ε_Z and ε_A, we considered E_f as functions of contributions from the edges and the inside atoms. For the Z and A nanoribbons, these

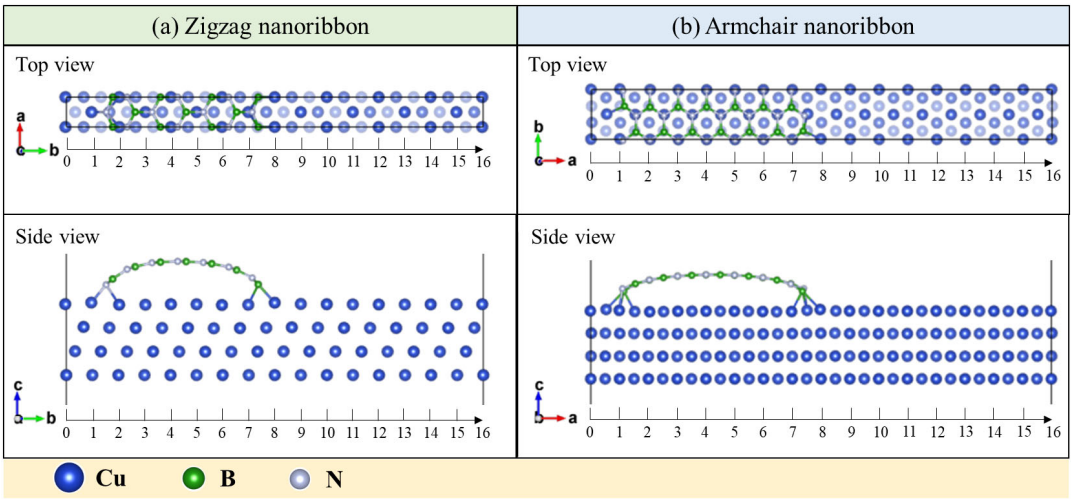

Figure 1: (a) Schematic of the optimized atomic structure of a zigzag nanoribbon hBN on Cu(111). The lateral periodicity of the unit cell is $1 \times 8\sqrt{3}$. (b) Schematic of the optimized atomic structure of an armchair nanoribbon hBN on Cu(111). The lateral periodicity of the unit cell is $16 \times \sqrt{3}$. Both (a) and (b) correspond to models with $n_t = 6$. Blue, green, and silver spheres represent Cu, B, and N atoms, respectively.

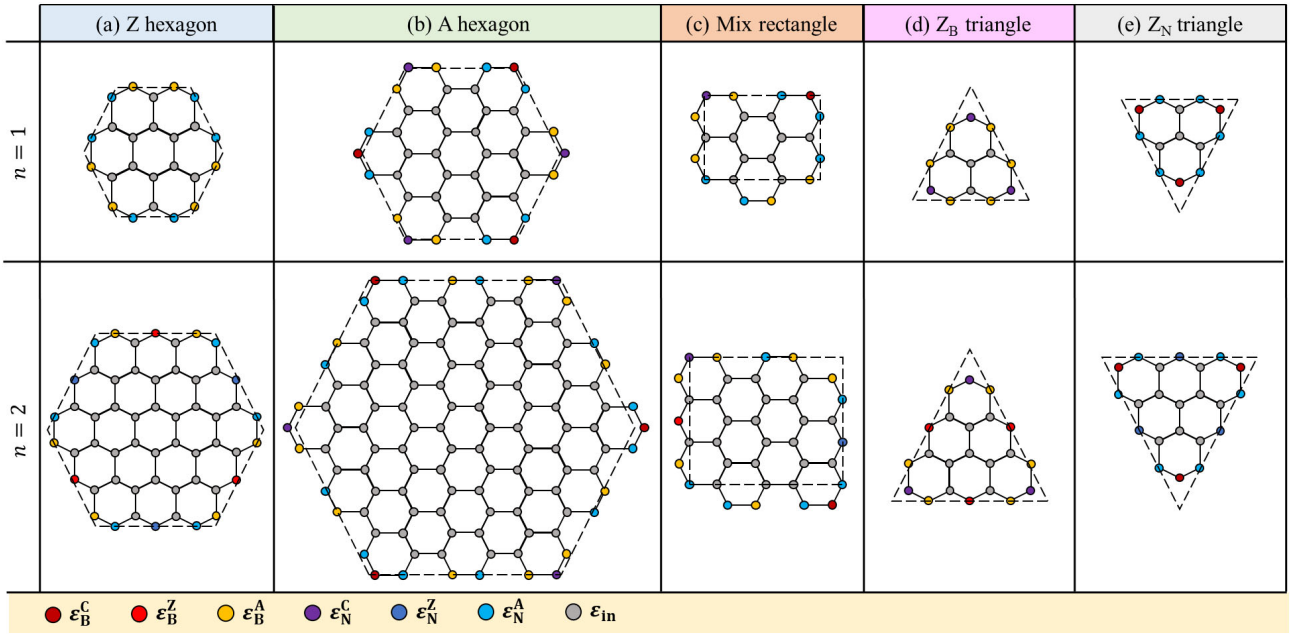

Figure 2: Schematic atomic structures of (a) Z hexagon, (b) A hexagon, (c) Mix rectangle, (d) Z_B triangle, and (e) Z_N triangle for $n = 1$ and $n = 2$. Brown, red, yellow, purple, blue, sky blue, and gray spheres represent atoms associated with ε_B^C, ε_B^Z, ε_B^A, ε_N^C, ε_N^Z, ε_N^A, and ε_{in}, respectively. The regions enclosed by dashed-lines indicate the boundaries used to predict the critical size.

were defined as

$$E_f = \varepsilon_Z + 2n_t\,\varepsilon_{in}^Z, \tag{4}$$

$$E_f = 2\varepsilon_A + 4n_t\,\varepsilon_{in}^A, \tag{5}$$

where ε_{in}^Z and ε_{in}^A are the energies per atom of the inside atoms for Z and A nanoribbons, respectively. By constructing Eqs. (4) and (5) for $n_t = 3$ to 13, the values of the ε_Z, ε_{in}^Z, ε_A, and ε_{in}^A were obtained as functions of nanoribbon width. It was hypothesized that for sufficiently wide nanoribbons, ε_Z and ε_A would converge, and $\varepsilon_{in}^Z = \varepsilon_{in}^A$, indicating consistent inside atoms energies for both Z and A nanoribbons.

B. Large island model

As the large island model, five specific shapes of hBN islands shown in Figure 2 were placed on Cu(111). The shapes were Z hexagons, an A hexagon, Z + A (Mix) rectangles, Zigzag B (Z_B) triangles, and Zigzag N (Z_N) triangles. The parameter n represents the size of the island as it grows while maintaining its shape. The results from nanoribbon calculations alone are insufficient to predict the critical sizes for a variety of island shapes. Thus, in addition to nanoribbons, we need to rely on the calculation results for hBN islands on Cu(111). To minimize the influence of the curl effect, the largest possible hBN islands were placed onto a sufficiently large Cu(111) unit cell.

A 10×10 hexagonal lateral supercell of Cu(111) was utilized with a super-slab geometry that included an 11 Å vacuum layer. The slab thickness consisted of three Cu layers, with the bottom Cu layer was fixed. The k-point mesh was set to $2 \times 2 \times 1$. Z_B and Z_N triangular islands corresponding to $n = 4$ to 6 were placed on the Cu(111) 10×10 supercell, and the calculations were performed. These atomic models are shown in Figure S2 in Supplementary Material.

To predict of critical sizes for various shapes, we calculated new variables. ε_B^Z and ε_N^Z represent the energies of B and N atoms constituting the Z edge, respectively. Similarly, ε_B^A and ε_N^A describe the energies of B and N atoms constituting the A edge. ε_B^C and ε_N^C indicate the energies of B and N atoms constituting the corners of hBN islands, which cannot be determined from the nanoribbon models. Here, $\varepsilon_Z = \varepsilon_B^Z + \varepsilon_N^Z$, $\varepsilon_A = \varepsilon_B^A + \varepsilon_N^A$, and $\varepsilon_C = \varepsilon_B^C + \varepsilon_N^C$.

The formation energies of Z_B and Z_N triangular islands can be expressed as follows:

$$E_f = 6\varepsilon_B^A + 3\varepsilon_N^C + 3(n-1)\varepsilon_B^Z + (n^2+3n)\varepsilon_{in}, \tag{6}$$

$$E_f = 6\varepsilon_N^A + 3\varepsilon_B^C + 3(n-1)\varepsilon_N^Z + (n^2+3n)\varepsilon_{in}. \tag{7}$$

From these equations, ε_Z was evaluated. By combining with the value of ε_A obtained from the nanoribbon models, ε_C was determined. It is anticipated that the value of ε_Z derived from the island calculations may not exactly match ε_Z obtained from the nanoribbon models. Therefore, careful consideration of this discrepancy is necessary in the discussion.

III. RESULTS AND DISCUSSION

A. Nanoribbon results

We evaluated E_f from the nanoribbon calculations under the conditions of $\Delta\mu_B = -8.01$ eV and $\Delta\mu_N = -6.34$ eV. These conditions correspond to $\bar{\mu}_N = 0.5$ in our previous study [29], and this specific point was chosen to enable a direct comparison with our previous results.

Figure 3(a) shows the n_t-dependence of ε_{in}^Z and ε_{in}^A. The values of $\varepsilon_B + \varepsilon_N$ and ε_{in} are our previous results [29]. As n_t

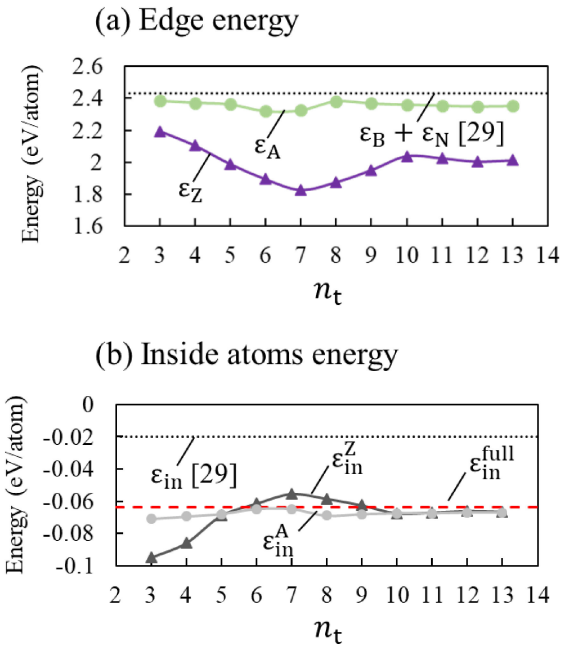

Figure 3: (a) Edge energies and (b) Inside atoms energies as functions of n_t under the conditions of $\Delta\mu_B = -8.01$ eV and $\Delta\mu_N = -6.34$ eV. Purple, light green, black, and gray markers represent ε_Z, ε_A, ε_{in}^Z, and ε_{in}^A, respectively. The dotted-lines indicate values from Ref. 29. The red dashed-line depicts ε_{in}^{full}, the ideal value of ε_{in} in our computation.

increases, both ε_Z and ε_A converge, along with ε_{in}^Z and ε_{in}^A. The converged values are $\varepsilon_Z = 2.01\,\mathrm{eV atom^{-1}}$, $\varepsilon_A = 2.35\,\mathrm{eV atom^{-1}}$, and $\varepsilon_{in}^Z = \varepsilon_{in}^A = -0.07\,\mathrm{eV atom^{-1}}$. The agreement between ε_{in}^Z and ε_{in}^A is consistent with our expectation, and we henceforth indicate this common value as $\varepsilon_{in} = -0.07\,\mathrm{eV atom^{-1}}$. These converged values differ from those obtained in our previous study, where $\varepsilon_B + \varepsilon_N = 2.43\,\mathrm{eV atom^{-1}}$ and $\varepsilon_{in} = -0.02\,\mathrm{eV atom^{-1}}$. In our previous study, only triangular islands were considered, and the curl effects led to an overestimation of ε_{in} in the positive direction, while $\varepsilon_B + \varepsilon_N$ was underestimated. Compared to the present results, ε_{in} was overestimated by $0.05\,\mathrm{eV atom^{-1}}$. Although $\varepsilon_B + \varepsilon_N$ was underestimated, its value is still larger than the converged values of ε_Z and ε_A. This overestimation occurs because that $\varepsilon_B + \varepsilon_N$ averages the contributions of ε_Z, ε_A, and corner effects. Since corners have higher energy, making them energetically disadvantageous. Additionally, ε_Z is more stable than ε_A, indicating that Z edge is more stable, and islands with Z edge are more likely to stabilize. The calculated values of ε_Z, ε_A, and ε_{in} derived from the nanoribbon models were used for predicting critical sizes, as described later.

Here, it must be noticed that the difference between the converged value of ε_{in} and $\varepsilon_{in}^{full} = -0.06\,\mathrm{eV atom^{-1}}$ is only $0.01\,\mathrm{eV atom^{-1}}$. This small discrepancy indicates that our approach based on the nanoribbon models sufficiently excludes curl effects [29]. Then, the evaluated values of ε_Z and ε_A must be also accurate enough. Overall, the edge energy and the inside atoms energy are expected to exhibit improved quantitative accuracy compared to our previous results.

B. Large island results

We calculated the total energies of triangular islands with $n = 4$ to 6 for Z_B and Z_N triangles on Cu(111) 10×10. From these results, E_f under the conditions of $\Delta\mu_B = -8.01$ eV and $\Delta\mu_N = -6.34$ eV was derived ε_B^Z, ε_N^Z, and ε_C were evaluated as 1.17, 0.97, and 3.94 eV, respectively. Note that the combined value $\varepsilon_B^Z + \varepsilon_N^Z = 2.14$ eV was 0.13 eV higher than the value $\varepsilon_Z = 2.01$ eV obtained from nanoribbon model calculations. It is considered that the discrepancy comes from the curl effect. Similarly, ε_C is also expected to deviate slightly from its true value in macroscopic islands. Therefore, it is crucial to interpret any predictions of critical sizes based on these values as approximate references.

The critical size of triangular islands can be predicted using Eqs. (6) and (7). From the calculation results of island, the n-independent terms $6\varepsilon_B^A + 3\varepsilon_N^C$ and $6\varepsilon_N^A + 3\varepsilon_B^C$ were determined. For $\Delta\mu_B = -8.01$ eV and $\Delta\mu_N = -6.34$ eV, these values were 12.97 and 12.95 eV, respectively. These values could be also expected to deviate slightly from the true ones.

C. Prediction of critical size

Utilizing the results from Sections III.A and III.B, we predicted the critical sizes of hBN islands with various shapes. Five specific shapes of hBN were considered: Z hexagon, A hexagon, Mix rectangle, Z_B triangle, and Z_N triangle [Figure 2(a–e)]. The critical sizes for Z hexagon, A hexagon, and Mix rectangle were predicted based on the following equations:

$$E_f = 6\varepsilon_A + 3(n-1)\varepsilon_Z + 6(n^2+n)\varepsilon_{in}, \quad (8)$$

$$E_f = 3\varepsilon_C + 6n\varepsilon_A + 6(3n^2+n)\varepsilon_{in}, \quad (9)$$

$$E_f = \varepsilon_C + (4+n)\varepsilon_A + (n-1)\varepsilon_Z + 2(n^2+3n+1)\varepsilon_{in}. \quad (10)$$

Since E_f is a quadratic function of ε_{in} in these equations, plotting E_f as the function of n, which determines the size of the hBN nucleus, yields convex curves. The value of n at the maximum E_f corresponds to the critical size.

Figure 4(a) shows the predicted critical sizes for the five shapes using Eqs. (6)–(10) under the conditions of $\Delta\mu_B = -8.01$ eV and $\Delta\mu_N = -6.34$ eV. To facilitate comparison, the islands size is normalized based on the area. The normalizing method is shown in Supplementary Material. Numerical values of the critical sizes for each shape are listed in Table 1. Under these conditions, Z hexagons were found to be the most energetically favorable and easiest to form. For triangular shapes, the critical sizes predicted here are approximately 1/7 to 1/4 of those reported in our previous work [29]. This discrepancy arises from the inability of the previous method to properly evaluate both edge and inside atoms energies, highlighting issues in its quantitative accuracy. Unfortunately, critical sizes are challenging to observe experimentally, and no experimental data exists for comparison as far as we examined. However, our method provides qualitative insights into the conditions required to fabricate high-quality and large-area hBN films by identifying the

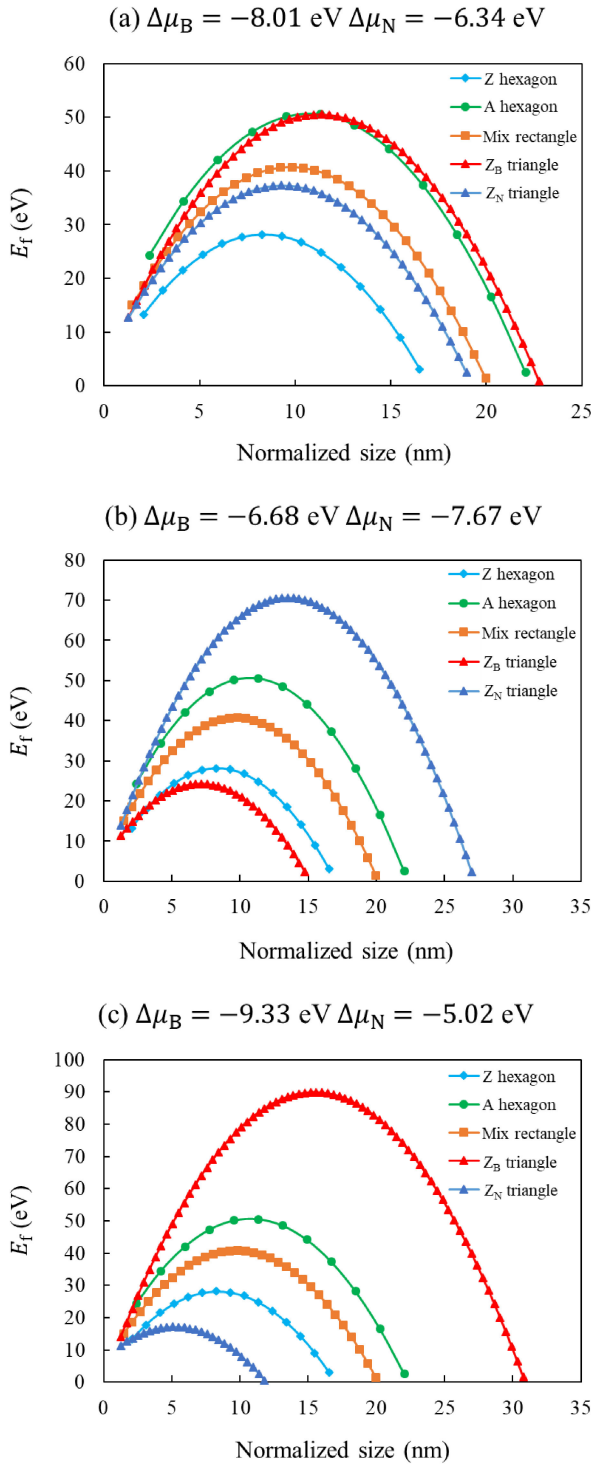

Figure 4: Formation energies E_f as functions of normalized size for Z hexagon, A hexagon, Mix rectangle, Z_B triangle, and Z_N triangle under the conditions of (a) $\Delta\mu_B = -8.01$ eV and $\Delta\mu_N = -6.34$ eV, (b) $\Delta\mu_B = -6.68$ eV and $\Delta\mu_N = -7.67$ eV, and (c) $\Delta\mu_B = -9.33$ eV and $\Delta\mu_N = -5.02$ eV.

energetically stable shapes and the chemical potential conditions under which critical sizes increase.

Figure 4(b, c) depicts E_f as the function of normalized size under the conditions $\Delta\mu_B = -6.68$ eV, $\Delta\mu_N = -7.67$ eV and $\Delta\mu_B = -9.33$ eV, $\Delta\mu_N = -5.02$ eV, respectively. These conditions correspond to the B-rich ($\overline{\mu}_N = 0$) and N-rich ($\overline{\mu}_N = 1.0$) scenarios as discussed in our previous study [29]. For $\Delta\mu_B = -6.68$ eV and $\Delta\mu_N = -7.67$ eV, Z_B triangle is the most stable across almost all normalized sizes. Conversely, for $\Delta\mu_B = -9.33$ eV and $\Delta\mu_N = -5.02$ eV, Z_N triangle is the most stable across all normalized sizes.

Table 1: Comparison of normalized critical sizes in unit of nm for Z hexagon, A hexagon, Mix rectangle, Z_B triangle, and Z_N triangle between this study and our previous study [29] under the conditions of $\Delta\mu_B = -8.01$ eV and $\Delta\mu_N = -6.34$ eV.

	This study	Ref. 29
Z hexagon	8.26	—
A hexagon	11.33	—
Mix rectangle	9.83	—
Z_B triangle	11.38	77.50
Z_N triangle	9.27	39.58

When the chemical potentials are constrained by $\mu_B + \mu_N = E_{BN}$, the curves for Z hexagon, A hexagon, and Mix rectangle in Figure 4 remain unchanged regardless of the chemical potential. This is because these three shapes have equal numbers of B and N atoms at their edge. To understand which chemical potential conditions, stabilize specific shapes and result in larger critical size, it is necessary to conduct free independent variation of $\Delta\mu_B$ and $\Delta\mu_N$ in Eqs. (2) and (3). This will be discussed in detail in Section III.E.

D. Comparison of predicted values and results derived from large island models

We examined the discrepancies between E_f predicted by Eqs. (6)–(10) and those derived from calculations of the large island models (hereafter referred to as the island results). Calculations were performed for Z hexagons with $n = 1$ to 3, an A hexagon with $n = 1$, Mix rectangles with $n = 1$ to 4, and Z_B and Z_N triangles with $n = 1$ to 6, within the limitation of the Cu(111) 10×10 unit cell. The atomic models for Z_B and Z_N triangles are shown in Figure S2 in Supplementary Material, while the models for Z hexagon, A hexagon, and Mix rectangle are shown in Figure S3.

Figure 5 compares E_f values predicted in Section III.C with the island results under the conditions of $\Delta\mu_B = -8.01$ eV and $\Delta\mu_N = -6.34$ eV. The numerical values of E_f are listed in Table S1 in Supplementary Material. For Z hexagons, the island results are higher than the predicted values, which can be attributed to the curl effect. This effect reduces the absolute value of ε_{in}, an averaged quantity that depends on the number of inside atoms and their distances to the Cu(111) surface. For a detailed discussion on the curl effect, refer to Ref. 29 and Figure S4 in Supplementary Material. Even when using the maximum feasible size within our computation limitation, the system exhibits such an effect. Further, regarding the initial rise in Figure 5, our prediction method fails to reproduce the island results.

The predicted values for Z hexagons can be derived solely from the results in Section III.A. In contrast, the values for

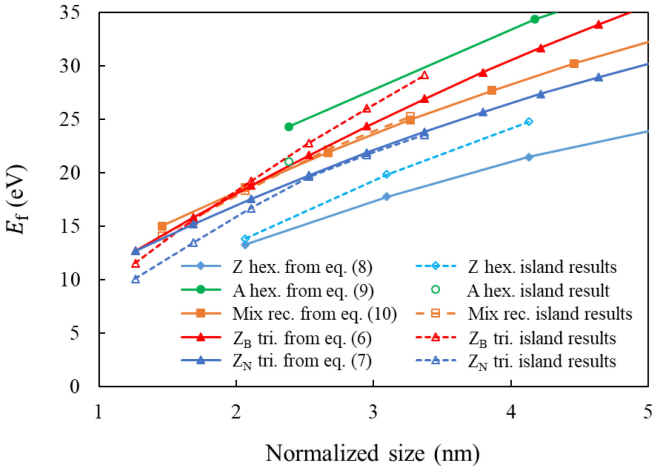

Figure 5: Formation energies E_f as the function of normalized size for Z hexagon, A hexagon, Mix rectangle, Z_B triangle, and Z_N triangle under the conditions of $\Delta\mu_B = -8.01$ eV and $\Delta\mu_N = -6.34$ eV. The solid-lines represent the predicted values evaluated from Eqs. (6)–(10), while the dashed-lines indicate the results derived from calculations of the large island models (the island results).

other four shapes must be the results of Section III.B as well as from Section III.A. For A hexagon, Eq. (9) includes $3\varepsilon_C$ term. The island results are lower than the predicted values, likely due to the overestimation of $3\varepsilon_C$, as discussed in Section III.A. For Mix rectangles, Eq. (10) includes ε_C term. While the predicted values appear to match the island results, this may come from an overestimation of ε_C and an underestimation of ε_{in}. In the case of Z_B triangles, the island results are lower than the predicted values for $n = 1$ and 2, but this trend reverses for $n \geq 3$. This reversal is likely due to an overestimation of the $6\varepsilon_B^A + 3\varepsilon_N^C$ term in Eq. (6). It may also be influenced by the curl effect and the increase in the number of inside atoms. For Z_N triangles, the island results are initially lower than the predicted values but almost agree for $n \geq 3$. This agreement is thought to come from the overestimation of the $6\varepsilon_N^A + 3\varepsilon_B^C$ term in Eq. (7). As with Z_B triangle, changes in the curves of the island results may also be influenced by the curl effect and the number of inside atoms. Overall, we confirmed that even for large islands on Cu(111) 10×10, the curl effect is evident. The variables derived from the island results tend to be overestimated.

E. 2D variation of the chemical potential

1. Most stable shape and critical size

We conducted a 2D analysis by freely varying both $\Delta\mu_B$ and $\Delta\mu_N$ in steps of -0.05 eV within the range of -10 eV, rather than using a one-dimensional range of chemical potentials as in previous scenarios. Figure 6(a) shows the $\Delta\mu_B$–$\Delta\mu_N$ phase diagram of the most stable shapes at their critical sizes, determined by E_f. The critical value n_c, which corresponds to the critical size, can be calculated for each shape by differentiating Eqs. (6)–(10) with respect to n. Within the range where $n_c \geq 1$, n_c was rounded to the nearest integer to one decimal place. The ranges of $\Delta\mu_B + \Delta\mu_N$

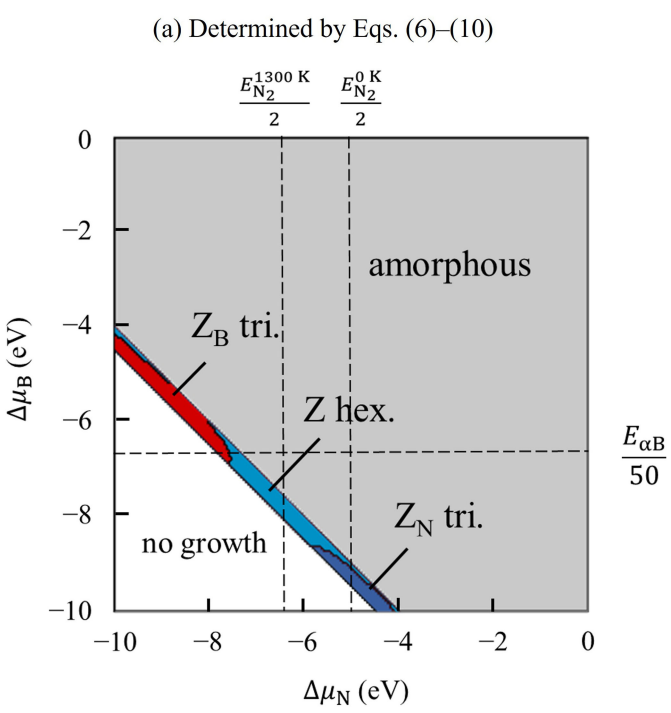

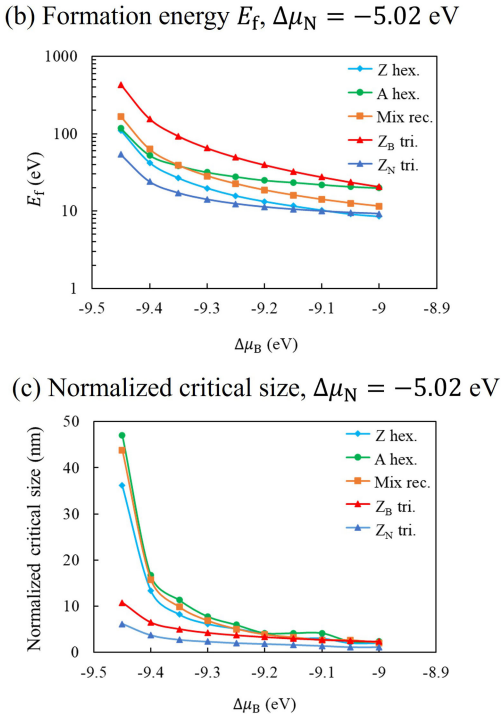

Figure 6: (a) $\Delta\mu_B$–$\Delta\mu_N$ phase diagram showing the most stable shape at the critical size. $E_{\alpha B}/50$, $E_{N_2}^{0\,K}/2$, and $E_{N_2}^{1300\,K}/2$ represent the energies of α-boron, N_2 molecules at 0 K, and N_2 molecules at 1300 K, respectively. Red, light blue, blue, gray, and uncolored regions depict Z_B triangle, Z hexagon, Z_N triangle, amorphous, and no growth phases, respectively. (b) Formation energies E_f and (c) normalized critical sizes as functions of $\Delta\mu_B$ for Z hexagon, A hexagon, Mix rectangle, Z_B triangle, and Z_N triangle under the condition of $\Delta\mu_N = -5.02$ eV.

where $n_c \geq 1$ for each shape are shown in Figure S5 in Supplementary Material. In the range where $n_c \geq 1$, the islands are assumed to grow, while in the range where $n_c < 1$, any nuclei, regardless of shape, are considered stable. This implies disordered growth, leading to the formation of an amorphous structure. Consequently, the boundary between the island growth and the amorphous-formation is located at $\Delta\mu_B + \Delta\mu_N = 14.00\,\text{eV}$. On the other hand, in regions where $\Delta\mu_B + \Delta\mu_N < -14.45\,\text{eV}$, ε_{in} takes a positive value, indicating that the critical size becomes infinite for any shape. This suggests that crystal growth is not possible in this region. In conclusion, the range of $\Delta\mu_B + \Delta\mu_N$ that allows for ordered growth of specific shapes is

$$-14.45\,\text{eV} \leq \Delta\mu_B + \mu_N \leq -14.00\,\text{eV}. \quad (11)$$

Within this range, only three shapes — Z hexagon, Z_B triangle, and Z_N triangle — are found to be the most stable.

In our proposed scenario, E_{Batom} ($\Delta\mu_B = 0$) represents the upper limit of μ_B, indicating chemical equilibrium with single B atoms along this line. Similarly, E_{Natom} ($\Delta\mu_N = 0$) represents the upper limit of μ_N, indicating chemical equilibrium with single N atoms along this line. When $\Delta\mu_B$ exceeds $E_{\alpha B}/50$, it is assumed to be in chemical equilibrium with single B atom gas. Similarly, when $\Delta\mu_N$ exceeds $E_{N_2}/2$, it is assumed to be in equilibrium with single N atom gas. When $\Delta\mu_B$ is below $E_{\alpha B}/50$, it is assumed to be in chemical equilibrium with α-boron. Similarly, when $\Delta\mu_N$ is below $E_{N_2}/2$, it is assumed to be in chemical equilibrium with N_2 molecules. Note that the chemical potential of N_2 molecules depends on temperature. In this study, $E_{N_2}^{0\,K}/2$ was obtained from DFT calculations, while $E_{N_2}^{1300\,K}/2$, corresponding to the typical experimental CVD growth temperature of 1300 K, was calculated using data from the NIST-JANAF Thermochemical Tables [35]. On the other hand, since α-boron is a solid, the effects of rotational and translational motions on its chemical potential can be neglected. Additionally, due to its highly covalent crystalline structure (rhombohedral configuration), the influence of lattice vibrations on the chemical potential at approximately 1300 K can be considered negligible [36]. Therefore, only the reference value obtained from DFT calculations was adopted. $E_{\alpha B}/50$, $E_{N_2}^{0\,K}/2$, and $E_{N_2}^{1300\,K}/2$ correspond to $\Delta\mu_B = -6.68\,\text{eV}$, $\Delta\mu_N = -5.02\,\text{eV}$, and $\Delta\mu_N = -6.41\,\text{eV}$, respectively [Figure 6(a)].

The most stable region for Z_B triangle is very limited at $\Delta\mu_B \leq -6.68\,\text{eV}$, and within $-6.41\,\text{eV} \leq \Delta\mu_N \leq -5.02\,\text{eV}$, the most stable structure varies between Z hexagon and Z_N triangle depending on $\Delta\mu_B$. Near $\Delta\mu_N = -6.41\,\text{eV}$, which corresponds to the assumed CVD growth temperature, Z hexagon is the only stable shape. It is worth noting that our scenario presupposes the formation of hBN and does not consider the formation of other compounds. Exploring the chemical potentials at which hBN transitions to other compounds lies beyond the scope of this study, but it would be an intriguing approach for discussing CVD growth environments.

Figure 6(b) shows E_f of each shape as the function of $\Delta\mu_B$ when $\Delta\mu_N$ is fixed at $-5.02\,\text{eV}$. Figure 6(c) describes the critical size of each shape instead of E_f. As $\Delta\mu_B$ decreases, E_f increases monotonically, resulting in larger critical sizes. Conversely, as $\Delta\mu_B$ increases, E_f decreases, and the critical size becomes smaller. For Z hexagon, A hexagon, and Mix rectangle, since the numbers of B and N atoms at the edge are equal, both E_f and the critical size remain constant under the condition of $\Delta\mu_B + \Delta\mu_N$ = constant. On the other hand, triangles have unequal numbers of B and N atoms at the edge, so E_f and the critical size do not remain constant. This behavior is shown in Figure S6 in Supplementary Material. The chemical potential conditions where triangles become the most stable in terms of E_f and exhibit the largest critical sizes are near the phase boundary between Z hexagon and triangles. In summary, to increase the critical size, it is necessary to adjust the chemical potential within the range specified by Eq. (11), moving closer to $\Delta\mu_B + \Delta\mu_N = -14.45\,\text{eV}$. Additionally, to form triangular nuclei with the larger critical size, the chemical potential should be as close as possible to the phase boundary with Z hexagon.

2. Generalization of shape scenario

In Section III.E.1, we established that the possible shapes of hBN nuclei are restricted to Z hexagon or one of the triangular shapes: Z_B or Z_N. Consequently, the stability comparison scenario between Z hexagons and triangles can be generalized. Moreover, in addition to the standard Z hexagon, we considered the stability of Z_B-like hexagon, characterized by a longer Z_B edge relative to the Z_N edge, and Z_N-like hexagon, where the Z_N edge is longer than the Z_B edge.

Figure 7(a) schematically illustrates our idea of shape generalization. In this framework, Z hexagon is formed by truncating the corners of Z_N triangle by Z_B triangles with side

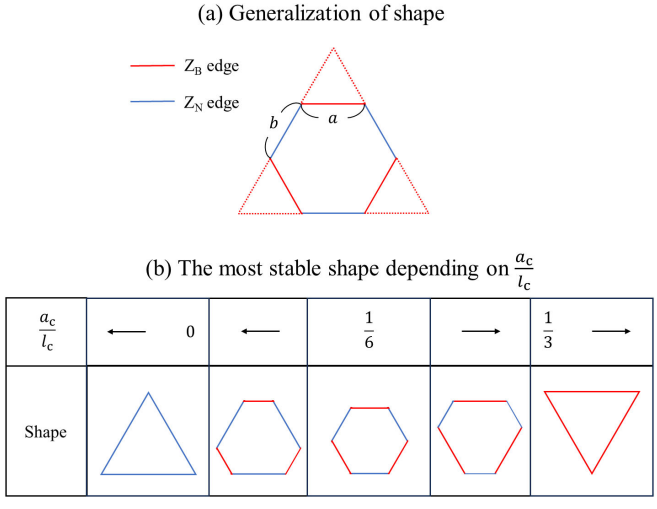

Figure 7: (a) Schematic illustration of the generalization idea, showing the transformation of an equilateral triangle into a hexagon. Red and blue lines indicate the Z_B and Z_N edges, respectively. *a* and *b* represent the length of the Z_B and Z_N edges, respectively. (b) Most stable shapes as the function of a_c/l_c. The Z_N triangle, Z_N-like hexagon, Z hexagon, Z_B-like hexagon, and Z_B triangle correspond to $a_c/l_c \leq 0$, $0 < a_c/l_c < 1/6$, $a_c/l_c = 1/6$, $1/6 < a_c/l_c < 1/3$, and $1/3 \leq a_c/l_c$, respectively.

length a. After truncation, the perimeter l of the resulting Z hexagon is given by $3a + 3b$, and its area is $(\sqrt{3}/4)(2a + b)^2 - (3\sqrt{3}/4)a^2$. Since a and b correspond to the lengths of the Z_B and Z_N edges, respectively, the edge energies per unit length, e_B and e_N, and the energy per unit are for inside atoms, e_{in}, can be calculated using the following equations:

$$e_B = \frac{\varepsilon_B^Z}{u}, \tag{12}$$

$$e_N = \frac{\varepsilon_N^Z}{u}, \tag{13}$$

$$e_{in} = \frac{4}{\sqrt{3}} \frac{\varepsilon_{in}}{u^2}, \tag{14}$$

where u represents the unit length of the edge. In this scenario, the smallest nuclei size is assumed to be the triangle at $n = 1$ [Figure 2(d, e)]. The area per hexagonal ring is 5.66 Å^2, resulting in this triangular hBN being 16.98 Å^2. Using this area, u was determined as $\sqrt{16.98 \times (4/\sqrt{3})} = 6.26$ Å. This value was used to evaluate e_B, e_N, and e_{in}.

Following the above, the formation energy of the hexagon can be expressed as:

$$E_f = 3ae_B + (l - 3a)e_N + \left[\frac{\sqrt{3}}{4}\left(a + \frac{l}{3}\right)^2 - \frac{3\sqrt{3}}{4}a^2\right]e_{in}. \tag{15}$$

Differentiating Eq. (15) with respect to a, setting the derivative to zero, and solving for the critical value of E_f, the critical value of a (a_c) can be obtained as:

$$a_c = \frac{\sqrt{3}}{e_{in}}(e_B - e_N) + \frac{l}{6}. \tag{16}$$

Substituting Eq. (16) into a in Eq. (15) and then differentiating with respect to l, setting the derivative to zero, and solving for the critical value of E_f, the critical value of l (l_c) can be derived as

$$l_c = -\frac{2\sqrt{3}}{e_{in}}(e_B + e_N), \tag{17}$$

where l_c is constrained to be $l_c \geq 18.79$ Å, the minimum nucleus size. The ratio a_c/l_c is then evaluated as

$$\frac{a_c}{l_c} = \frac{2e_N - e_B}{3(e_B + e_N)}. \tag{18}$$

This idea allows for a generalization of this shape theory. Depending on the chemical potential range, the most stable shape corresponding to Eq. (18) can be categorized as follows: $a_c/l_c \leq 0$ (Z_N triangle), $0 < a_c/l_c \leq 1/6$ (Z_N-like hexagon), $a_c/l_c = 1/6$ (Z hexagon), $1/6 < a_c/l_c \leq 1/3$ (Z_B-like hexagon), and $1/3 \leq a_c/l_c$ (Z_B triangle) [Figure 7(b)].

Figure 8(a) shows the $\Delta\mu_B$–$\Delta\mu_N$ phase diagram where $l_c \geq 18.79$ (Å), indicating the most stable shape at l_c. The possible presence range of l_c is

$$-14.45\,\text{eV} \leq \Delta\mu_B + \Delta\mu_N \leq -13.35\,\text{eV}. \tag{19}$$

The ranges of $\Delta\mu_B$ and $\Delta\mu_N$, where the Z_B triangle, Z_B-like hexagon, Z_N-like hexagon, and Z_N triangle are the most stable shapes under the condition of Eq. (19), are summarized in Table 2. Here, the range where the Z hexagon becomes the most stable corresponds to the boundary region between the most stable ranges of the Z_B-like hexagon and the Z_N-like hexagon.

Thus far, we have considered scenarios where the shape of the hBN nucleus is determined by its critical size. However, we also examined the case where the shape is determined not by the critical size, but by the diffusion length of the growth precursor. Although the exact growth precursor is unknown, it can be assumed to be monomers of B or N. In the case where the shape is determined by the critical size, the islands

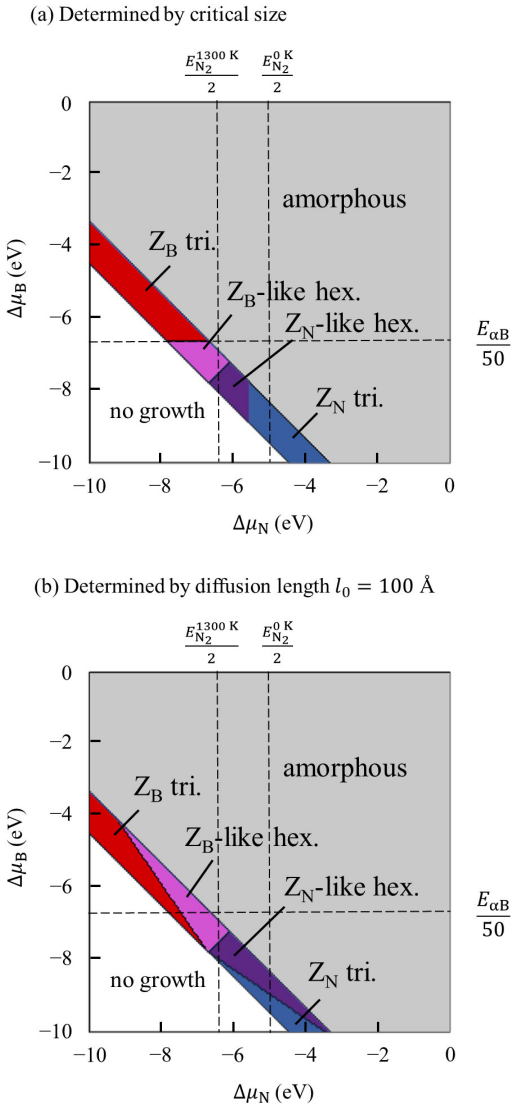

Figure 8: $\Delta\mu_B$–$\Delta\mu_N$ phase diagrams showing the most stable shape, determined by (a) the critical size and (b) the diffusion length $l_0 = 100$ Å. $E_{\alpha B}/50$, $E_{N_2}^{0\,K}/2$, and $E_{N_2}^{1300\,K}/2$ represent energies of α-boron, N_2 molecule at 0 K, and N_2 molecule at 1300 K, respectively. Red, pink, purple, blue, gray, and uncolored regions depict Z_B triangle, Z_B hexagon, Z_N hexagon, Z_N triangle, amorphous, and no growth phases, respectively.

Table 2: Summary of the most stable ranges of $\Delta\mu_B$ (eV) and $\Delta\mu_N$ (eV) for Z_B triangle, Z_B-like hexagon, Z_N-like hexagon, and Z_N triangle, determined by most stable shape at critical size under the condition of Eq. (19).

	$\Delta\mu_B$	$\Delta\mu_N$
Z_B triangle	$-6.60 \le \Delta\mu_B \le -3.35$	$-10.0 \le \Delta\mu_N \le -6.75$
Z_B-like hexagon	$-7.75 \le \Delta\mu_B \le -6.60$	$-7.80 \le \Delta\mu_N \le -6.15$
Z_N-like hexagon	$-8.85 \le \Delta\mu_B \le -7.25$	$-6.65 \le \Delta\mu_N \le -5.55$
Z_N triangle	$-10.0 \le \Delta\mu_B \le -7.80$	$-5.55 \le \Delta\mu_N \le -3.35$

Table 3: Summary of the most stable ranges of $\Delta\mu_B$ (eV) and $\Delta\mu_N$ (eV) for Z_B triangle, Z_B-like hexagon, Z_N-like hexagon, and Z_N triangle, determined by the most stable shape at diffusion length $l_0 = 100$ Å under the condition of Eq. (19).

	$\Delta\mu_B$ and $\Delta\mu_N$	$\Delta\mu_B$	$\Delta\mu_N$
Z_B triangle	$\Delta\mu_B \le -1.46\ \Delta\mu_N - 17.57$	$-7.65 \le \Delta\mu_B \le -3.35$	$-10.0 \le \Delta\mu_N \le -6.80$
Z_B-like hexagon	$\Delta\mu_B > -1.46\ \Delta\mu_N - 17.57$	$-7.65 \le \Delta\mu_B \le -4.20$	$-9.15 \le \Delta\mu_N \le -6.15$
Z_N-like hexagon	$\Delta\mu_B > -0.68\ \Delta\mu_N - 12.35$	$-10.0 \le \Delta\mu_B \le -7.25$	$-6.65 \le \Delta\mu_N \le -3.35$
Z_N triangle	$\Delta\mu_B \le -0.68\ \Delta\mu_N - 12.35$	$-10.0 \le \Delta\mu_B \le -7.85$	$-6.65 \le \Delta\mu_N \le -3.35$

and the precursor must be in complete equilibrium. However, since islands can grow continuously over time, assuming an arbitrarily long diffusion length is unrealistic. Therefore, we consider that the shape is determined by the diffusion length. If we consider that the shape of the hBN nucleus is determined by a diffusion length $l_0 = 100$ Å, the values of a at the critical value of E_f and the ratio of l_0 to a_0 are given by:

$$a_0 = \frac{\sqrt{3}}{e_{in}}(e_B - e_N) + \frac{100}{6}, \tag{20}$$

$$\frac{a_0}{l_0} = \frac{\sqrt{3}}{100 e_{in}}(e_B - e_N) + \frac{1}{6}. \tag{21}$$

Figure 8(b) indicates the $\Delta\mu_B$–$\Delta\mu_N$ phase diagram for the most stable shapes, assuming the hBN nucleus shape is determined by $l_0 = 100$ Å. The range of hBN growth is the same as in Eq. (19). The phase boundaries between the Z_B triangle and Z_B-like hexagon, and Z_N triangle and Z_N-like hexagon are not perfectly linear, respectively. However, for simplicity, these boundaries are approximated as linear equations. The equations of the linear lines for the boundaries between Z_B triangle and Z_B-like hexagon, and Z_N triangle and Z_N-like hexagon, are $\Delta\mu_B = -1.46\Delta\mu_N - 17.57$ eV and $\Delta\mu_B = -0.68\Delta\mu_N - 12.35$ eV, respectively. The ranges of $\Delta\mu_B$ and $\Delta\mu_N$ where the Z_B triangle, Z_B-like hexagon, Z_N-like hexagon, and Z_N triangle are the most stable under the condition of Eq. (19) are summarized in Table 3. The most stable range for the triangle depends on the diffusion length. If l_0 is shorter than 100 Å, the most stable range becomes wider, while it narrows as l_0 become longer. This behavior is shown in Figure S7 in Supplementary Material.

We have examined the regions where the triangle shapes are most stable in both scenarios: one where the hBN nucleus shape is determined by the critical size, and the other by diffusion length. Considering both scenarios, the most stable shapes within the range satisfying Eq. (19) are as follows: Z_B triangle is the most stable in the range $\Delta\mu_B \le -1.46\Delta\mu_N - 17.57$ eV, $-6.60\,\text{eV} \le \Delta\mu_B \le -3.35$ eV, and $-10.0\,\text{eV} \le \Delta\mu_N \le -6.75$ eV, while Z_N triangle is most stable in the range $\Delta\mu_B \le -0.68\Delta\mu_N - 12.35$ eV, $-10.0\,\text{eV} \le \Delta\mu_B \le -7.80$ eV, and $-5.55\,\text{eV} \le \Delta\mu_N \le -3.35$ eV.

F. Discussions

First, we examine whether the three issues identified our previous study [29] and, described in Section I, have been addressed. The three issues are as follows: 1) The three variables could only predict the critical size for hBN nuclei in the shape of a triangle. 2) These variables include effects specific to small islands, which have not been fully examined, and there should be concern about the quantitative validity of these three variables. 3) The range of chemical potentials used in the analysis of the results was one-dimensional, allowing for only limited comparison with experimental results. To address the first issue, we successfully predicted the critical sizes of non-triangular shapes by evaluating ε_Z, ε_A, ε_B^Z, ε_N^Z, ε_C, and ε_{in} through calculations of nanoribbon hBN on Cu(111) and large hBN islands on Cu(111) 10×10. Our findings indicate that hBN nuclei stabilize energetically as either Z hexagons or triangles. This is supported by the greater stability of ε_Z compared to ε_A and the strong dependence of ε_B^Z and ε_N^Z on the chemical potential. For the second issue, we calculated sufficiently wide hBN nanoribbons, confirming that ε_{in} reaches the value equivalent to ε_{in}^{full}. The edge energies ε_Z and ε_A have been accurately estimated. To address the third issue, we allowed the chemical potential to vary freely in 2D using Eqs. (2) and (3). This approach enabled us to construct $\Delta\mu_B$–$\Delta\mu_N$ phase diagrams for the most stable shapes, providing more detailed data. We identified that the specific chemical potential conditions are required to reach the critical size for growing high-quality single crystals.

In typical CVD experiments, hBN islands on Cu(111) are frequently reported to grow into triangular shapes [10, 14, 19–21, 23–26]. According to our results, the formation of triangular islands requires chemical potential conditions that

are either B-rich and N-poor or N-rich and B-poor. It is thus essential to determine which of these conditions is present during growth. Our independent calculations indicate that B atoms are energetically more stable in subsurface sites than on the outermost surface of Cu(111), whereas N atoms are more stable on the surface than in subsurface sites [29]. These findings are shown in Figure S8 in Supplementary Material, align with experimental observation of B atom dissolutions into transition metals, including Cu, at high temperatures [37–39]. Based on this evidence, we infer that B atoms dissolve into the Cu substrate, creating a B-poor condition at the surface. While, N atoms do not dissolve into Cu, resulting in an N-rich condition at the surface. According to our results, the B-poor and N-rich conditions correspond to the stability region of Z_N triangle. We therefore propose that the triangular hBN islands observed in experiments are Z_N triangles.

In contrast, experiments using a small amount of O_2 mixed with Ar carrier gas (Ar with 0.5% O_2) yield nearly perfect hexagonal hBN islands on Cu(111) [26]. We hypothesize that this occurs because O_2 reacts with N atoms to form gaseous products, which then leaves the Cu surface. Consequently, μ_N shifts slightly towards the N-poor side, aligning with the stability range of the Z hexagon identified in our results. Furthermore, Cu substrates subjected to electropolishing are oxidized on the surface, and hBN islands grown on such substrates are also observed to form hexagonal shapes [19]. We propose that the surface oxidation prevents B atoms from entering subsurface sites, resulting a more uniform chemical potential ratio of B and N on the surface. This condition corresponds to the stability region of Z hexagon in our results. Based on these findings, we infer that the observed hexagonal hBN islands are Z hexagons. Additionally, non-CVD methods of hBN production shows N atoms being substituted with O atoms [40], further suggesting that O_2 plays a role in hBN growth.

The three phase diagrams we constructed are all qualitatively valid, as they consistently explain the experimental observations without contradiction. Across all three diagrams, the lower-left region (B-poor and N-poor directions) corresponds to the no-growth phase, while the upper-right region (B-rich and N-rich directions) consistent with the amorphous phase. Even in the growth phase, in the lower-left region of the phase diagram, where the critical size becomes significantly large, the system exhibits similar shapes within qualitatively nearly the same range of chemical potential. This is because ε_{in} is more stable than ε_B^Z and ε_N^Z.

However, notable differences exist among the three phase diagrams. These differences are reflected in the slope of the phase boundaries and the width of the growth regions. The variations arise from whether the Z edge, A edge, and corners are considered collectively or whether only the Z edge is accounted for. They depend on whether the shape is dictated by the critical size or the diffusion length. The difference between the phase diagrams in Figures 6(a) and 8(a) lies in the consideration of corner instability in triangular shapes, as accounted for in Figure 6(a). Consequently, Z hexagons without corners become more stable for small islands. This is further influenced by the assumption for Figure 8(a) that the shape of a small island is determined solely by ε_B^Z and ε_N^Z. The difference between the phase diagrams in Figure 8(a, b) is attributed to the fact that, as islands grow beyond their critical sizes, the influence of ε_B^Z and ε_N^Z diminishes in Figure 8(b). If experimental or theoretical advancements enable the precise determination of the actual chemical potential in experiments, it may become possible to identify which of the phase diagrams is most appropriate.

Furthermore, some challenges remain. The values of ε_B^Z, ε_N^Z, ε_C, and the combined corner energies of the triangles, $6\varepsilon_B^A + 3\varepsilon_N^C$ and $6\varepsilon_N^A + 3\varepsilon_B^C$, were estimated based on the calculations of hBN islands. As a result, these values are slightly overestimated, though not critically so. Consequently, the E_f and critical sizes of triangular islands are also overestimated. To improve the quantitative accuracy of these variables, more advanced analytical methods are required. Addressing this issue remains a subject for future work.

In this study, we assumed that the chemical potential has 2D degrees of freedom. As evident from Figures 6(a) and 8(a, b), the largest critical size is achieved outside the conventional range of the chemical potential, where it was previously considered to have only one degree of freedom. Furthermore, as discussed above, various experimental studies have likely been conducted outside this conventional one-dimensional range as well. These findings support the idea that, in hBN growth, the chemical potential indeed has 2D degrees of freedom. This means that the supply of B and N is independent rather than correlated, and that their precursors also behave independently.

More fundamentally, we assumed growth on a clean terrace without considering the effects of steps. Nucleation is believed to occur at defects or steps. Indeed, step-flow growth of hBN on metal surfaces has been observed experimentally [10, 13, 15, 21, 25], and DFT calculations have reported that steps stabilize edge energies [10]. Further, we assumed that, under high-temperature conditions, H desorbs from the Cu surface, and thus excluded H from our calculations. As a result, the effects of H during hBN growth were not addressed. Considering these two factors could lead to deeper insights into the CVD growth mechanism of hBN, but this is beyond the scope of this study and remains a subject for future work.

IV. CONCLUSIONS

In this study, we performed DFT calculations to predict the critical sizes of non-triangular shapes and improve the accuracy of edge energies quantification for hBN on the Cu(111) terrace. Specifically, we calculated hBN nanoribbons with Z edges, nanoribbons with A edges, and larger hBN islands on Cu(111). First, by obtaining ε_{in} without the curl effect, we successfully calculated edge energies with enough precision. Additionally, we achieved the prediction of critical sizes for shapes that had not been previously analyzed. On the other hand, we found that the E_f of small hBN islands on Cu(111)

are strongly influenced by curl effects. Subsequently, by varying the chemical potential in 2D, we clarified that the most stable structures at the critical size are three types: Z-hexagonal, Z_B-triangular, and Z_N-triangular. Furthermore, we generalized the shapes and depicted two new types of phase diagrams. These results demonstrate that the stability of hBN island shapes is highly dependent on the chemical potential. Additionally, we identified that to increase the critical size, the chemical potential should be as close as possible to $\Delta\mu_B + \Delta\mu_N = -14.45$ eV. Our findings provide an explanation for the correspondence between the observed hBN island shapes on the Cu(111) surface during CVD experiments and their respective chemical potential conditions. Furthermore, we proposed optimal chemical potential conditions for growing hBN films with superior single crystallinity.

Acknowledgments

This study is partially supported by KAKENHI (21H01394 and 21H01768). This research used the supercomputer of Institute for Solid State Physics (ISSP) at the University of Tokyo and ISSP, Univ. of Tokyo, and the supercomputer Fugaku of RIKEN. Atomic models are depicted using the Visualization for Electronic and Structural Analysis (VESTA).

Appendix

Detailed computational models and theoretical considerations of this paper are available in Supplementary Material at https://doi.org/10.1380/ejssnt.2025-018.

Note

This paper was presented at the 10th International Symposium on Surface Science, Kitakyushu International Conference Center, Fukuoka, Japan, 20–24 October, 2024.

References

[1] K. Watanabe, T. Taniguchi, and H. Kanda, Nat. Mater. **3**, 404 (2004).
[2] T. Taniguchi and K. Watanabe, J. Cryst. Growth **303**, 525 (2007).
[3] Z. Liu, L. Song, S. Zhao, J. Huang, L. Ma, J. Zhang, J. Lou, and P. M. Ajayan, Nano Lett. **11**, 2032 (2011).
[4] L. Britnell, R. V. Gorbachev, R. Jalil, B. D. Belle, F. Schedin, M. I. Katsnelson, L. Eaves, S. V. Morozov, A. S. Mayorov, N. M. R. Peres, A. H. C. Neto, J. Leist, A. K. Geim, L. A. Ponomarenko, and K. S. Novoselov, Nano Lett. **12**, 1707 (2012).
[5] C. R. Dean, A. F. Young, I. Meric, C. Lee, L. Wang, S. Sorgenfrei, K. Watanabe, T. Taniguchi, P. Kim, K. L. Shepard, and J. Hone, Nat. Nanotechnol. **5**, 722 (2010).
[6] J. Xue, J. Sanchez-Yamagishi, D. Bulmash, P. Jacquod, A. Deshpande, K. Watanabe, T. Taniguchi, P. Jarillo-Herrero, and B. J. LeRoy, Nat. Mater. **10**, 282 (2011).
[7] X. Cui, G.-H. Lee, Y. D. Kim, G. Arefe, P. Y. Huang, C.-H. Lee, D. A. Chenet, X. Zhang, L. Wang, F. Ye, F. Pizzocchero, B. S. Jessen, K. Watanabe, T. Taniguchi, D. A. Muller, T. Low, P. Kim, and J. Hone, Nat. Nanotechnol. **10**, 534 (2015).
[8] T. Uwanno, T. Taniguchi, K. Watanabe, and K. Nagashio, ACS Appl. Mater. Interfaces **10**, 28780 (2018).
[9] K. Takeyama, R. Moriya, K. Watanabe, S. Masubuchi, T. Taniguchi, and T. Machida, Appl. Phys. Lett. **117**, 153101 (2020).
[10] T.-A. Chen, C.-P. Chuu, C.-C. Tseng, C.-K. Wen, H.-S. P. Wong, S. Pan, R. Li, T.-A. Chao, W.-C. Chueh, Y. Zhang, Q. Fu, B. I. Yakobson, W.-H. Chang, and L.-J. Li, Nature **579**, 219 (2020).
[11] S. Fukamachi, P. Solís-Fernández, K. Kawahara, D. Tanaka, T. Otake, Y.-C. Lin, K. Suenaga, and H. Ago, Nat. Electron. **6**, 126 (2023).
[12] Y. Uchida, S. Nakandakari, K. Kawahara, S. Yamasaki, M. Mitsuhara, and H. Ago, ACS Nano **12**, 6236 (2018).
[13] K. Y. Ma, L. Zhang, S. Jin, Y. Wang, S. I. Yoon, H. Hwang, J. Oh, D. S. Jeong, M. Wang, S. Chatterjee, G. Kim, A-R. Jang, J. Yang, S. Ryu, H. Y. Jeong, R. S. Ruoff, M. Chhowalla, F. Ding, and H. S. Shin, Nature **606**, 88 (2022).
[14] K. K. Kim, A. Hsu, X. Jia, S. M. Kim, Y. Shi, M. Hofmann, D. Nezich, J. F. Rodriguez-Nieva, M. Dresselhaus, T. Palacios, and J. Kong, Nano Lett. **12**, 161 (2012).
[15] J. Lu, P. S. E. Yeo, Y. Zheng, H. Xu, C. K. Gan, M. B. Sullivan, A. H. C. Neto, and K. P. Loh, J. Am. Chem. Soc. **135**, 2368 (2013).
[16] G. Kim, A-R. Jang, H. Y. Jeong, Z. Lee, D. J. Kang, and H. S. Shin, Nano Lett. **13**, 1834 (2013).
[17] C. M. Orofeo, S. Suzuki, H. Kageshima, and H. Hibino, Nano Res. **6**, 335 (2013).
[18] Y. Gao, W. Ren, T. Ma, Z. Liu, Y. Zhang, W.-B. Liu, L.-P. Ma, X. Ma, and H.-M. Cheng, ACS Nano **7**, 5199 (2013).
[19] R. Y. Tay, M. H. Griep, G. Mallick, S. H. Tsang, R. S. Singh, T. Tumlin, E. H. T. Teo, and S. P. Karma, Nano Lett. **14**, 839 (2014).
[20] Y. Ji, B. Calderon, Y. Han, P. Cueva, N. R. Jungwirth, H. A. Alsalman, J. Hwang, G. D. Fuchs, D. A. Muller, and M. G. Spencer, ACS Nano **11**, 12057 (2017).
[21] L. Wang, X. Xu, L. Zhang, R. Qiao, M. Wu, Z. Wang, S. Zhang, J. Liang, Z. Zhang, Z. Zhang, W. Chen, X. Xie, J. Zong, Y. Shan, Y. Guo, M. Willinger, H. Wu, Q. Li, W. Wang, P. Gao, S. Wu, Y. Zhang, Y. Jiang, D. Yu, E. Wang, X. Bai, Z.-J. Wang, F. Ding, and K. Liu, Nature **570**, 91 (2019).
[22] M. Petrović, M. Horn-von Hoegen, and F.-J. Meyer zu Heringdorf, Sci. Rep. **9**, 19553 (2019).
[23] S. Wang, J. Crowther, H. Kageshima, H. Hibino, and Y. Taniyasu, ACS Nano **15**, 14384 (2021).
[24] Y. Fan, X. Liu, J. Yin, W. Lin, J. Li, B. Wu, Y. Wu, C. Zhang, and J. Kang, Cryst. Growth Des. **23**, 7789 (2023).
[25] H.-U.-P. Nguyen, S.-S. Wani, R.-H. Cyu, B. Rehman, M. Chaudhary, T.-Y. Yang, Y.-C. Hsu, K. M. M. D. K. Kimbulapitiya, Y.-R. Kuo, K. H. Aksu, L.-P.-N. Tran, V.-Q. Le, Y.-H. Chu, P.-W. Chiu, and Y.-L. Chueh, Chem. Mater. **36**, 2721 (2024).
[26] J. Li, A. Samad, Y. Yuan, O. Wang, M. N. Hedhili, M. Lanza, U. Schwingenschlögl, I. Abate, D. Akinwande, Z. Liu, B. Tian, and X. Zhang, Nat. Commun. **15**, 8589 (2024).
[27] R. Zhao, F. Li, Z. Liu, and F. Ding, Phys. Chem. Chem. Phys. **17**, 29327 (2015).
[28] Z. Zhang, Y. Liu, Y. Yang, and B. I. Yakobson, Nano Lett. **16**, 1398 (2016).
[29] R. Imamura and H. Kageshima, Jpn. J. Appl. Phys. **63**, 04SP39 (2024).
[30] PHASE/0 homepage, https://azuma.nims.go.jp (last accessed: 3 April, 2025).
[31] I. Hamada, Phys. Rev. B **91**, 119902 (2015).
[32] F. Schulz and P. Liljeroth, Phys. Rev. Mater. **3**, 084001 (2019).
[33] J. E. Northrup and S. Froyen, Phys. Rev. Lett. **71**, 2276 (1993).
[34] F.-H. Wang, P. Krüger, and J. Pollmann, Phys. Rev. B **64**,

035305 (2001).
[35] NIST-JANAF Thermochemical Tables, https://janaf.nist.gov/tables/N-023.html (last accessed: 3 April, 2025).
[36] A. Masago, K. Shirai, and H. Katayama-Yoshida, Phys. Rev. B **73**, 104102 (2006).
[37] R. Wu, I. K. Drozdov, S. Eltinge, P. Zahl, S. Ismail-Beigi, I. Božović, and A. Gozar, Nat. Nanotechnol. **14**, 44 (2019).
[38] K. M. Omambac, M. Petrović, P. Bampoulis, C. Brand, M. A. Kriegel, P. Dreher, D. Janoschka, U. Hagemann, N. Hartmann, P. Valerius, T. Michely, F. J. Meyer zu Heringdorf, and M. Horn-von Hoegen, ACS Nano **15**, 7421 (2021).
[39] P. Sutter and E. Sutter, Chem. Mater. **33**, 8838 (2021).
[40] M. Niibe, K. Miyamoto, T. Mitamura, and K. Mochiji, J. Vac. Sci. Technol. A **28**, 1157 (2010).